nature biomedical engineering

ARTICLES

https://doi.org/10.1038/s41551-018-0254-6

A designer self-assembled supramolecule amplifies macrophage immune responses against aggressive cancer

Ashish Kulkarni[1,2,3*], Vineethkrishna Chandrasekar[1,7], Siva Kumar Natarajan[1,7], Anujan Ramesh[2], Prithvi Pandey[4], Jayashree Nirgud[1], Harshangda Bhatnagar[1], Driti Ashok[1], Amrendra Kumar Ajay[1] and Shiladitya Sengupta[1,5,6*]

Effectively activating macrophages that can 'eat' cancer cells is challenging. In particular, cancer cells secrete macrophage colony stimulating factor (MCSF), which polarizes tumour-associated macrophages from an antitumour M1 phenotype to a pro-tumorigenic M2 phenotype. Also, cancer cells can express CD47, a 'don't eat me' signal that ligates with the signal regulatory protein alpha (SIRPα) receptor on macrophages to prevent phagocytosis. Here, we show that a supramolecular assembly consisting of amphiphiles inhibiting the colony stimulating factor 1 receptor (CSF-1R) and displaying SIRPα-blocking antibodies with a drug-to-antibody ratio of 17,000 can disable both mechanisms. The supramolecule homes onto SIRPα on macrophages, blocking the CD47–SIRPα signalling axis while sustainedly inhibiting CSF-1R. The supramolecule enhances M2-to-M1 repolarization within the tumour microenvironment, and significantly improves antitumour and antimetastatic efficacies in two aggressive animal models of melanoma and breast cancer, with respect to clinically available small-molecule and biologic inhibitors of CSF-1R signalling. Simultaneously blocking the CD47–SIRPα and MCSF–CSF-1R signalling axes may constitute a promising immunotherapy.

Macrophages form one of the first lines of defense in our 'innate' immune system and can phagocytose cancer cells[1]. However, macrophages also constitute a large fraction of the tumour stroma in nearly all cancers, and are associated with a poor prognosis[2–6]. This contradiction is explained by the existence of macrophages across a continuum of phenotypic and functional states, where the two ends of the continuum are defined as M1 and M2[7,8]. M1 macrophages mount a pro-inflammatory cytokine response, are involved in efficient antigen presentation and promote T helper type 1 (T_H1) cell response, all of which inhibit tumour progression. By contrast, M2 macrophages are associated with a predominantly anti-inflammatory cytokine response[9]. Cancer cells create a microenvironment that is enriched in signals that skew the tumour-associated macrophages (TAMs) towards an M2-like lineage, which promotes tumour progression and metastasis, angiogenesis and can suppress antitumour immune responses[3,10,11]. Depletion of TAMs, or skewing the M2/M1 ratio towards the M1 lineage, have emerged as attractive therapeutic goals in the treatment of cancer[1,12,13]. For example, cancer cells secrete macrophage colony stimulating factor (MCSF), which drives TAM recruitment and differentiation to an M2 phenotype by binding to the tyrosine kinase CSF-1R expressed on monocytes and macrophages[11]. While inhibition of CSF-1R signalling can deplete TAMs and enable the M1 polarization, two challenges can limit the efficacy of CSF-1R inhibitors[12]. First, there is a need to inhibit CSF-1R in a temporally sustained manner. Second, cancer cells express an 'eat me not' signal, CD47, which binds to SIRPα on macrophages and inhibits phagocytosis[14,15] (Fig. 1a), thus making an M2-to-M1 switch redundant.

We rationalized that these challenges can be addressed by designing a modular bifunctional therapeutic that can block the SIRPα–CD47 interaction and simultaneously inhibit CSF-1R. Similar concepts have been used to inspire the design of bifunctional antibodies or antibody drug conjugates, where different parts of the construct have distinct functions[16,17]. In a recent study, we demonstrated an alternative strategy, where two distinct molecular building blocks are designed to assemble into a single structure via supramolecular interactions[18] (Fig. 1b). We proposed that such a supramolecule could utilize the SIRPα-targeting component for binding to macrophages and block the 'eat me not' signal, while enabling a sustained shutdown of the CSF-1R-signalling pathway, which could skew the TAM M1/M2 ratio towards an M1 phenotype (Fig. 1b). Such a bifunctional supramolecule should then result in an efficient innate immune response against the tumour.

Results

Computationally simulating a stable supramolecule. As the first step, we designed an amphiphilic molecular subunit that could assemble into a supramolecular structure via hydrophobic–hydrophilic interactions. In a recent study, we described an algorithm based on quantum-mechanical, all-atomistic simulations to design these amphiphiles, starting from a known chemical backbone that blocked the molecular target[18,19]. The quantum-mechanical energy-minimized structure of an amphiphile with a CSF-1R-inhibiting

[1]Division of Engineering in Medicine, Department of Medicine, Brigham and Women's Hospital, Harvard Medical School, Boston, MA, USA. [2]Department of Chemical Engineering, University of Massachusetts, Amherst, MA, USA. [3]Center for Bioactive Delivery, Institute for Applied Life Sciences, University of Massachusetts, Amherst, MA, USA. [4]India Innovation Research Center, Invictus Oncology, New Delhi, India. [5]Dana Farber Cancer Institute, Boston, MA, USA. [6]Harvard-MIT Division of Health Sciences and Technology, Cambridge, MA, USA. [7]These authors contributed equally: Vineethkrishna Chandrasekar, Siva Kumar Natarajan. *e-mail: akulkarni@engin.umass.edu; shiladit@mit.edu

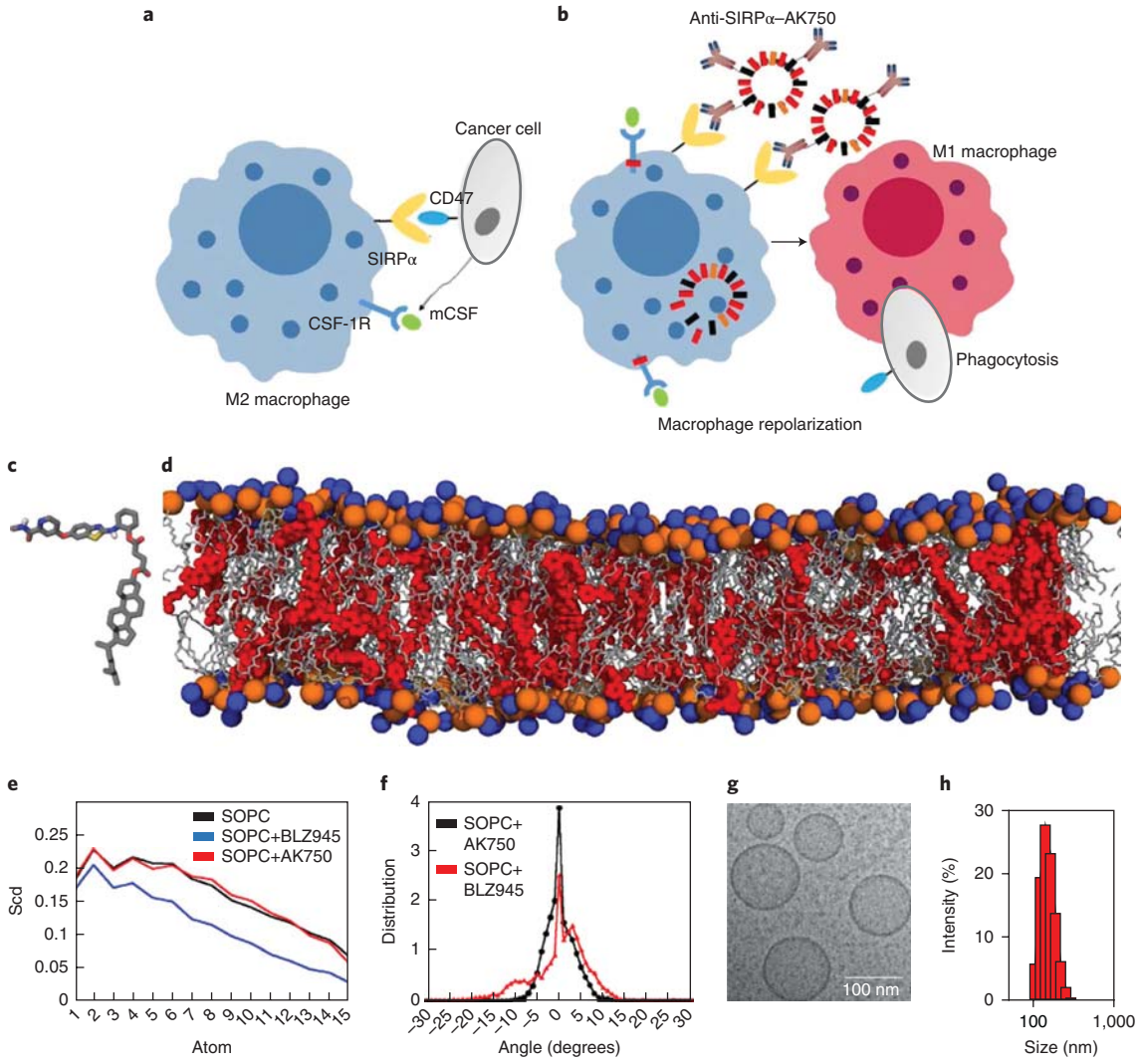

Fig. 1 | Design of a TAM-targeting supramolecular therapeutic. a, Schematic shows that cancer cells exploit CSF-1R signalling to polarize macrophages to the immunosuppressive 'M2' phenotype and SIRPα–CD47 interactions to inhibit phagocytosis. **b**, Schematic illustration of efficient repolarization of an M2 macrophage to the effector 'M1' phenotype by dual-function supramolecular therapeutic (anti-SIRPα–AK750)-mediated sustained inhibition of CSF-1R signalling and enhanced phagocytosis of cancer cells following inhibition of SIRPα. **c**, Representation of the quantum-mechanical-optimized structure of the molecular subunit of the supramolecular nanostructure, AK750. **d**, Snapshot of an all atomistic simulation of the molecular subunit (in red) interacting with the lipid bilayer at 100 ns shows a stable supramolecular structure; lipid (1-stearoyl-2-oleoyl-*sn*-glycero-3-phosphocholine (SOPC)) hydrophilic heads are shown in orange and blue spheres, and lipid tails are shown in grey. **e**, The angle between a vector defined on the C–C bond of the SOPC tail with the *z* axis (axis perpendicular to bilayer plane) is depicted as θ. Deuterium order parameter (Scd) is calculated using θ. Scd is calculated on each carbon atom of the phospholipid tail. Scd increases with lipid tail ordering. The deuterium order parameter on each methylene group of the saturated tail of the co-lipid is depicted. Lipid tail ordering is smallest for the BLZ945-containing lipid bilayer. Lipid tail ordering of the AK750 bilayer is similar to that of the pure lipid bilayer. **f**, Tilt angle is the angle between a vector joining the centres of mass of phospholipid tails and the *z*-axis (axis perpendicular to the bilayer plane). The value of tilt angle is positive or negative depending on the direction of the ripple. Its value is close to 0° when no ripples form. Distribution of tilt angle averaged over final 5 ns of the MD trajectory. A broader distribution and larger tilt angle indicate a higher extent of bilayer instability. **g**, High-resolution cryo-TEM image of AK750 showing the size of ~100 nm and spherical morphology. **h**, The size distribution (hydrodynamic diameter) of a representative batch of AK750 as measured by dynamic light scattering. The descriptions of panels **c**–**g** are adapted from ref. [19].

pharmacophore is shown in Fig. 1c. Our previous studies have revealed that such amphiphiles form bilayers with co-lipids, resulting in a supramolecular structure in the nanoscale[18]. Unlike nanoparticles or liposomes, where the drug is loaded in a carrier matrix and are rarely stable beyond 5 mol% drug, the supramolecular assembly means that we could achieve excellent stability of the structures at >20 mol% of the amphiphile[18,19]. Indeed, an all-atomistic simulation of a lipid bilayer containing 20 mol% of CSF-1R-inhibiting amphiphile revealed the formation of a stable supramolecular structure, termed AK750 (Fig. 1d). Analysis of the deuterium order parameter, that is ordering of the lipid tail, as a measure of stability[18], revealed that the amphiphile resulted in a lipid tail ordering that was consistent with a pure lipid bilayer (Fig. 1e). We measured ripple formation as a second measure of instability, which was quantified as the 'tilt' angle between a vector joining the centre of mass of phospholipid tails and the *z*-axis (axis perpendicular to bilayer plane). A tilt angle of 0° means no ripples were formed, while a broad distribution indicates a large tilt angle and high bilayer instability. As shown in Fig. 1f, the AK750 bilayer showed a narrow distribution around a tilt angle of 0°, which further validated the putative stability of the

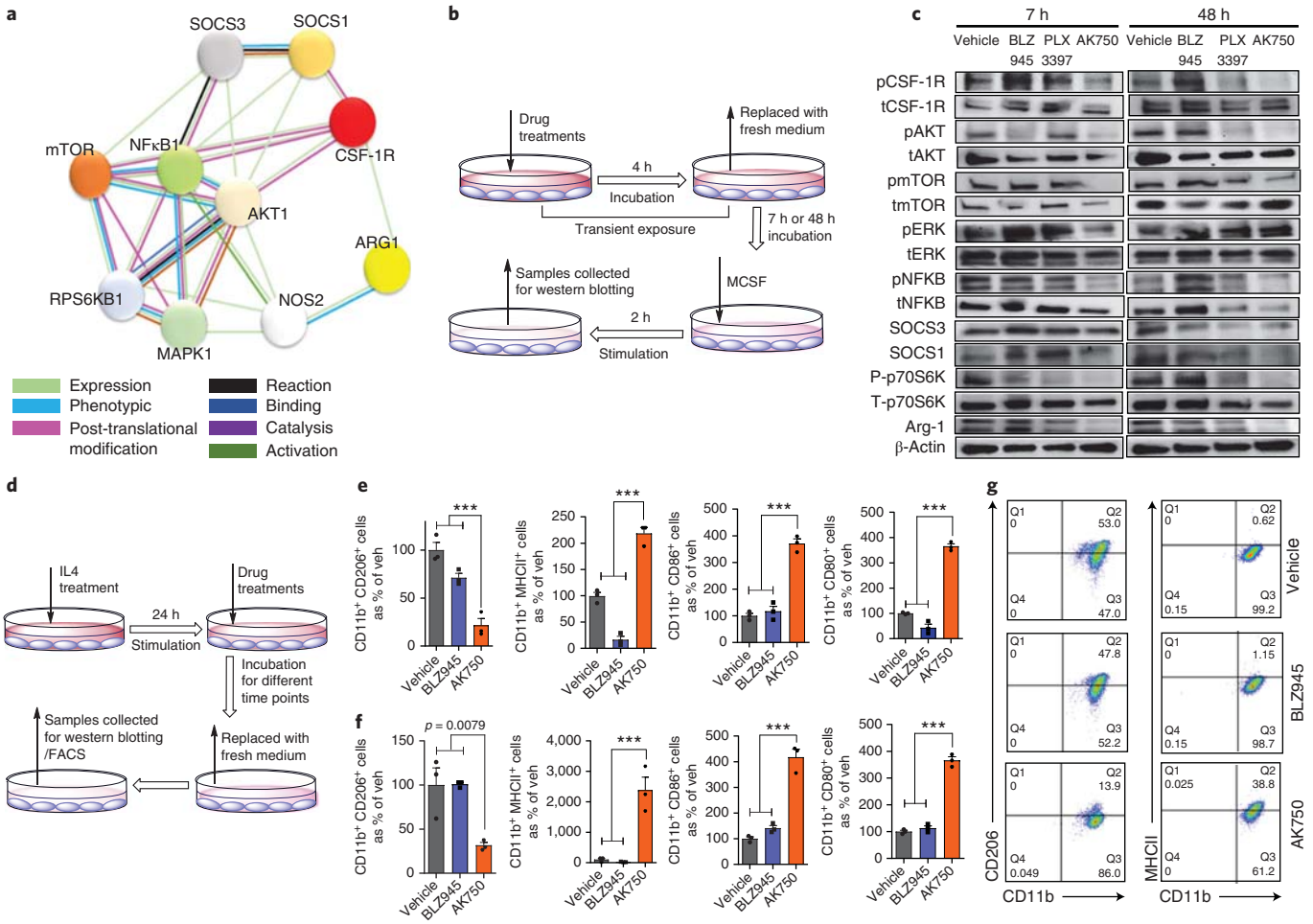

Fig. 2 | AK750 inhibits CSF-1R and downstream signalling pathways in a sustained manner, and efficiently repolarizes M2 macrophages to the M1 phenotype. a, STRING map showing different direct or indirect protein interactions associated with the CSF-1R signalling pathway in macrophages. The STRING map was generated using STRING database v. 10.0. **b**,**c**, Schematic representation of CSF-1R pathways inhibition assay (**b**). RAW264.7 macrophage cells were pre-treated with either BLZ945, PLX3397 or AK750 for 4 h, and then washed with cold PBS to remove the drugs that are not internalized. After 7 h or 48 h of recovery in fresh medium, the cells were stimulated with MCSF for 2 h. The cells were then washed and analysed for activation of signalling pathways, by western blotting for phosphor-CSF-1R, total CSF-1R and downstream signalling pathways (**c**). The cropped blots are used in the figure, and full-length blots are presented in Supplementary Fig. 13. **d**, Schematic representation of macrophage repolarization assay. RAW264.7 macrophages were stimulated with IL4 for 24 h, and then treated with either BLZ945, PLX3397 or AK750 for 12 h before the medium was replaced with fresh medium. The cell lysates were collected at different timepoints for western blotting and FACS. **e**,**f**, Quantification of flow cytometry data demonstrating expression of M2 markers ($CD11b^+CD206^+$), or M1 markers ($CD11b^+$, MHC-II, $CD86^+CD80^+$). The data shown are at 12 h (**e**) and 72 h (**f**) time points. Statistical analysis was performed with one-way ANOVA with Newman–Keuls post test. Data show mean ± s.e.m. ($n = 3$); $^{***}p < 0.001$. **g**, Flow cytometry demonstrating expression of $CD11b^+CD206^+$, $CD11b^+$MHC-II^+, $CD11b^+CD86^+$ and $CD11b^+CD80^+$ on the macrophages at the 72 h time point following different treatments.

supramolecular assembly. By contrast, simulating the behaviour of a classical CSF-1R inhibitor, BLZ945, in a lipid bilayer exhibited instability (Supplementary Fig. 1a,b), with decreased lipid tail ordering and broad distribution of the tilt angle as compared to the supramolecular structure (Fig. 1e,f). An analysis of the position of the centre of mass of the amphiphile relative to the head group of the co-lipid revealed that the pharmacophore is closer to the phospholipid head group while the hydrophobic tail anchors into the lipid bilayer, thus conferring the stability to the structure, unlike BLZ945, which sits close to the surface of the bilayer (Supplementary Fig. 1c,d).

CSF-1R-inhibiting amphiphile forms a stable supramolecule. Based on this theoretical understanding, we synthesized the amphiphiles by derivatizing the pharmacophore with a cholesterol anchor via a succinic acid linker (Supplementary Fig. 2a,b). Consistent with the theoretical predictions, the amphiphile formed a stable supramolecular assembly with co-lipids, phosphatidylcholine and pegylated-distearoylethanolamine (PEG-DSPE). The rationale for choosing the latter is that it can be derivatized with a SIRPα-blocking antibody at the terminal end of PEG, thus conferring modularity to the design of the bifunctional supramolecule. The phospholipid end co-assembles the lipid bilayer with the amphiphile. Cryo-transmission electron microscopy revealed that the supramolecular structures were spherical with a diameter of 109.4 ± 32.7 nm (Fig. 1g). Dynamic laser light scattering revealed a hydrodynamic radius of 175 ± 15 nm, while the zeta potential was measured to be −35 ± 7.8 mV (Fig. 1h, Supplementary Fig. 2c). Both size and zeta potential remained consistent over 30 days, which indicated that the supramolecular structures are indeed stable (Supplementary Fig. 2c). Additionally, we observed a sustained release of the drug from the supramolecular structure when incubated with tumour cell lysate, with greater stability at

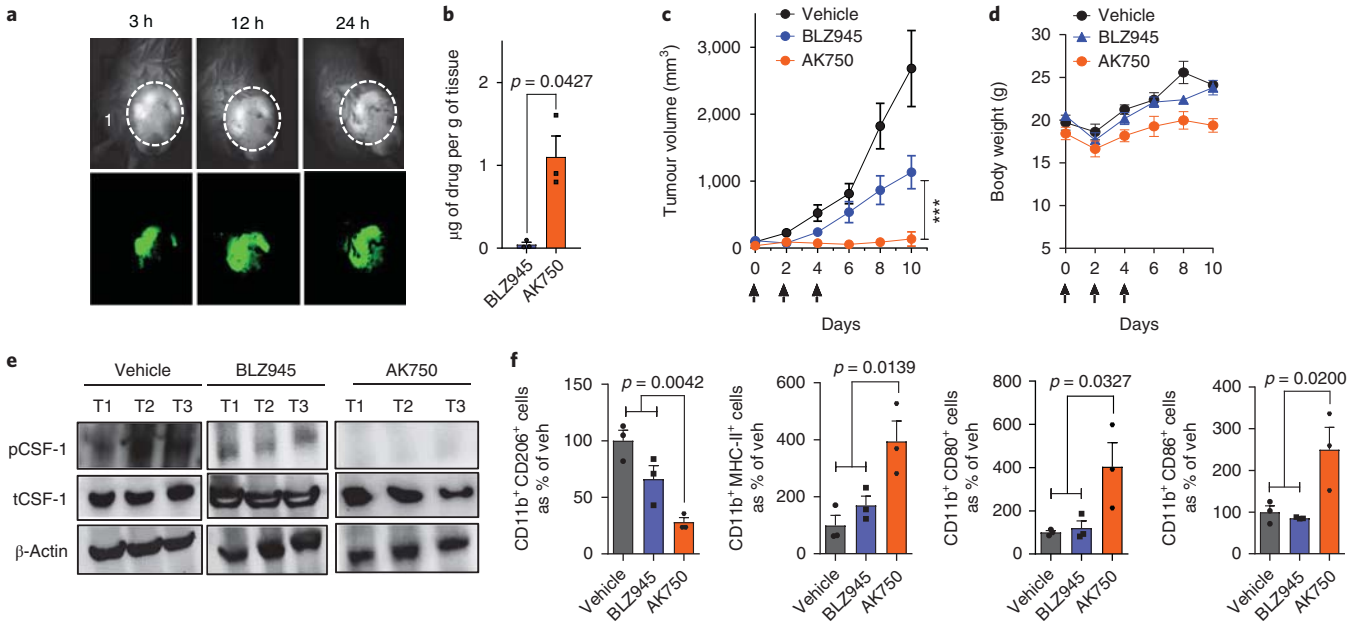

Fig. 3 | In vivo efficacy of AK750 in a syngeneic B-16/F10 melanoma C57BL/6 mice model. a, Representative images showing the temporal accumulation of a NIR dye-tagged AK750 in the tumour in a melanoma-bearing mouse model. **b**, Quantification of actual drug concentration reaching the tumour, in vivo, as measured using LC-MS. Tumour-bearing animals were injected with equimolar doses of the drugs. Data are mean ± s.e.m. ($n = 3$), statistical analysis performed with a Student's *t*-test, two-sided. **c**, Tumour growth curves show the effect of different treatments on tumour volume. Each animal was injected with three doses of either vehicle (control group), 45 mg kg^{-1} of free BLZ945, and AK750 (at an equimolar dose to BLZ945) on day 0 (first day of treatment), day 4 and day 8. Treatment with AK750 was significantly more effective than BLZ945. One should note the different routes of administration; intraperitoneal (i.p.) administration can result in lower bioavailability than intravenous (i.v.) administration. Data shown are mean ± s.e.m. ($n = 5$), ***$p < 0.001$ (one-way ANOVA). **d**, Drug toxicity assessed by measurements in overall body weight. Data shown are mean ± s.e.m. ($n = 5$). **e**, Western blot showing expression of phosphor-CSF-1R and total CSF-1R in three representative tumours of each treatment group, in vivo. Cropped blots are used here and full-length blots are presented in Supplementary Fig. 14. **f**, Graphs show the quantification of expression of different M2 markers ($CD11b^+CD206^+$), or M1 markers ($CD11b^+MHC\text{-}II^+$, $CD11b^+CD86^+$ and $CD11b^+CD80^+$) in single-cell suspensions of the harvested tumour post-treatment, as quantified using flow cytometry. Tumours were harvested on day 10 and single-cell suspensions were prepared. Data shown are mean ± s.e.m. ($n = 3$), *p* values are shown in the graphs. Statistical analysis was performed with one-way ANOVA with the Newman–Keuls post-hoc test.

physiological pH 7.4 (Supplementary Fig. 2d). Indeed, as in the case of antibody–drug conjugates, the stability of the construct at physiological pH and increased release in the tumour environment is a desirable characteristic that facilitates clinical success. Consistent with the computational simulation, we were unable to construct a stable nanostructure with 20 mol% of BLZ945.

AK750 enables sustained inhibition of CSF-1R signalling. Prior to introducing the SIRPα-binding functionality, we first validated that the supramolecule (AK750) indeed inhibits CSF-1R signalling. A robust and sustained activation of CSF-1R was observed in RAW-264.7 macrophage cells as early as 20 min following incubation with 10 ng ml^{-1} of MCSF (Supplementary Fig. 3a). We incubated the macrophages with the inhibitors for defined periods and then exposed the cells to MCSF for 20 min before analysing the phosphorylation status of CSF-1R using western blotting (Supplementary Fig. 3b). As shown in Supplementary Fig. 3c,d, the inhibitory effects of AK750 on CSF-1R were longer-lasting compared with BLZ945. An early and late rebound phosphorylation of CSF-1R was observed with BLZ945 treatment, which could result from a feedback loop and the kinase being replenished, respectively, and is likely minimized by the sustained effect of AK750. A similar effect was observed previously with phosphatidylinositol 3 kinase (PI3K) inhibitors[20]. We next developed a string map of the direct and indirect protein interactions with CSF-1R (Fig. 2a), and studied the effects of different CSF-1R inhibitors on these proteins. The macrophages were incubated with AK750, BLZ945 or PLX3397 for 4 h, and then exposed to MCSF for 2 h after a washout period of either 7 h (early time point) or 48 h (late time point) (Fig. 2b). This allowed us to delineate the key pathways and dissect the persistent effects of the treatments post drug-washout. Both BLZ945 and PLX3397 are currently in clinics for treatment of solid tumours[21]. As shown in Fig. 2c, AK750 exhibited a greater and sustained inhibition of phosphorylation of CSF-1R, and was effective in inducing a complete inhibition even at 48 h. Interestingly, the downstream signalling pathway that was dominantly ablated in a sustained manner by AK750, but not by BLZ945 and PLX3397, was the AKT–mTOR–p70S6K pathway. This is consistent with recent observations that PI3K acts as a macrophage switch between immune stimulation and suppression by inhibiting macrophage inflammatory responses[21]. We did not observe any effect on the mitogen activated protein kinase signalling pathway, although it is implicated in CSF-1R signalling. Additionally, AK750 resulted in a sustained, high suppressor of cytokine signalling 3 (SOCS3)/SOCS1 ratio compared with BLZ945 and PLX3397. In human tumours, expression of SOCS3 is associated with an M1 polarizing environment and tumour kill, while SOCS1-expressing macrophages support tumour survival[22]. Compared with other treatments, AK750-treated macrophages also exhibited the highest inducible NOS (iNOS)/Arginase-1 ratio, which is a hallmark of M1 macrophages[23]. SOCS1 is implicated in PI3K activity, which can mediate Arginase-1 expression in M2 macrophages, whereas SOCS3 blocks PI3K signalling[22,24]. Additionally, reverse transcription–polymerase chain reaction (RT–PCR) analysis revealed an increased IL12 and decreased IL10 expression in the macrophages following AK750 treatment as compared with BLZ945 and PLX3397 treatment (Supplementary Fig. 4a). These results indicated

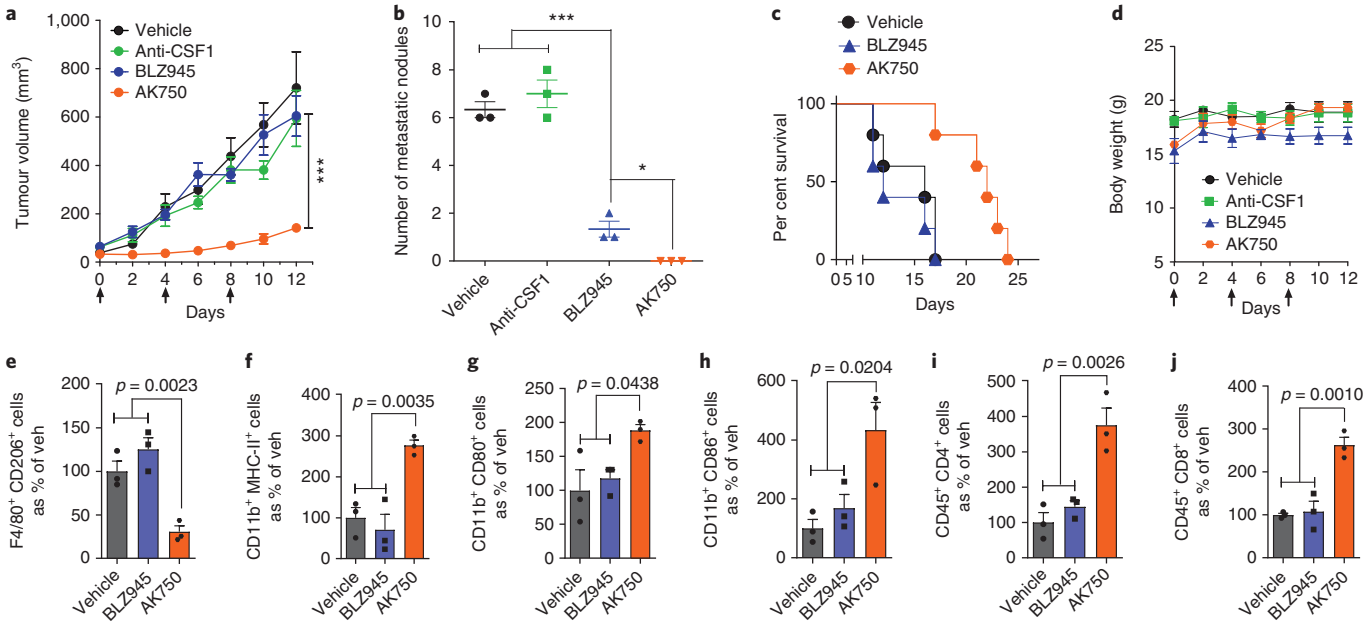

Fig. 4 | AK750 induces significant tumour growth inhibition in a syngeneic 4T1 breast cancer BALB/c mice model. a, Growth curves show the effect of different multi-dose treatments on tumour volume in 4T1 tumour-bearing mice. Each animal was injected with three doses of either vehicle (control), 45 mg kg^{-1} of free BLZ945, AK750 (at equimolar dose to BLZ945) or a CSF-1 neutralizing antibody (25 mg kg^{-1}) on day 0, day 4 and day 8. Data shown are mean ± s.e.m. ($n = 5$), ***$p < 0.001$ (one-way ANOVA). **b**, Number of metastatic nodules present in the lungs. Lungs were harvested from treated tumour-bearing mice on day 12, washed with cold PBS, and the number of metastatic nodules were counted. BLZ945 showed a reduction as compared to CSF-1 neutralizing antibody and the vehicle control. However, AK750 displayed complete inhibition of formation of metastatic nodules. Data shown are mean ± s.e.m. ($n = 3$), *$p < 0.05$; ***$p < 0.001$ (ANOVA followed by Newman–Keul post-hoc test). **c**, Kaplan–Meir survival curves show that treatment with AK750 increases survival ($p < 0.05$) as compared with BLZ945 ($n = 5$ in each treatment group). One should note that i.p. administration can result in lower bioavailability than i.v. administration. **d**, Drug toxicity assessed by measurements in overall body weight. Data shown are mean ± s.e.m. ($n = 5$). **e–j**, Quantification of expression of different M2 markers (CD11b$^+$CD206$^+$), M1 markers (CD11b$^+$MHC-II$^+$, CD11b$^+$CD86$^+$ and CD11b$^+$CD80$^+$), and effector T cell markers (CD45$^+$CD4$^+$, CD45$^+$CD8$^+$) in single-cell suspension of the harvested tumour post-treatment, as quantified using flow cytometry. Tumours were harvested on day 12 and single-cell suspensions were prepared. Data shown are mean ± s.e.m. ($n = 3$), p values are shown in the graphs. Statistical analysis was performed with one-way ANOVA with the Newman–Keuls post-hoc test.

that the blockade of CSF-1R-signalling using AK750 polarizes the naive macrophages to M1 status.

AK750 skews macrophages towards an M1 phenotype. Treatment with the lymphokine IL4 can polarize a macrophage to an M2 state independent of CSF1 signalling[25]. This offered the opportunity to test whether the sustained inhibition of CSF-1R afforded by AK750 could repolarize an M2 macrophage to an M1-like state, which cannot be probed by current short-acting inhibitors. We incubated the macrophages with IL4 for 24 h to skew the macrophages to an M2 state, and then added AK750 or BLZ945 for 4 h. The cells were then washed, and maintained in fresh media for 12–72 h. At different time-points, we harvested the cells and analysed the population for M1 (MHCII$^+$, CD86$^+$, CD80$^+$) or M2 (CD206$^+$) markers using fluorescence-activated cell sorting (Fig. 2d). As shown in Fig. 2e–g and Supplementary Figs. 4,5, treatment with AK750 resulted in a significant reduction in the M2 phenotype and increase in M1 macrophages as early as 12 h, which was sustained even at 72 h. We did observe a reduction in M2 markers with BLZ945 at early time-points, consistent with recent findings[13], but this effect was lost at later time points. The incubation with BLZ945 did not increase the M1 markers. The fluorescence-activated cell sorting (FACS) results were validated by western blotting, which revealed that treatment with AK750 resulted in the highest SOCS3/SOCS1 and iNOS/Arg-1 ratios, indicating a skew towards M1 macrophage status. Mechanistically, AK750 reduced the baseline CSF-1R activation and downstream PI3K signalling. Quantification of intracellular drug levels revealed that although both drugs reached equal levels at 4 h, at 18 h we observed a higher concentration of the molecular subunit of AK750 (Supplementary Fig. 6a), which together with the sustained release of the active drug from the supramolecule can potentially explain the sustained inhibitory effects of AK750 leading to repolarization of M2 macrophages to M1.

AK750 inhibits modulatory effects of tumour microenvironment. Cancer cells create a tumour microenvironment (TME), including secreting MCSF, which allows them to manipulate the TAMs towards a growth-enabling M2 status. Indeed, as shown in Supplementary Fig. 6b, we observed that the addition of B16/F10 melanoma-conditioned media to macrophages results in activation of CSF-1R, which is inhibited by AK750 in a sustained manner. The addition of tumour-conditioned media also decreased the iNOS signal in macrophages (Supplementary Fig. 6c), consistent with an M2 switch, which was inhibited by AK750 but not by BLZ945 (Supplementary Fig. 6d). Furthermore, quantification of the iNOS/Arg-1 ratio confirmed that AK750 increased the M1/M2 ratio despite the presence of tumour-conditioned media as compared with BLZ945 (Supplementary Fig. 6e). These results suggest that AK750 can inhibit the modulatory effects of the TME on macrophages. A similar decrease in the M2 lineage occurred when we incubated monocytes isolated from bone marrow with AK750 compared with BLZ945 in the presence of CSF1 (Supplementary Fig. 7). Neither BLZ945 nor AK750 induced any apoptosis or necrosis of

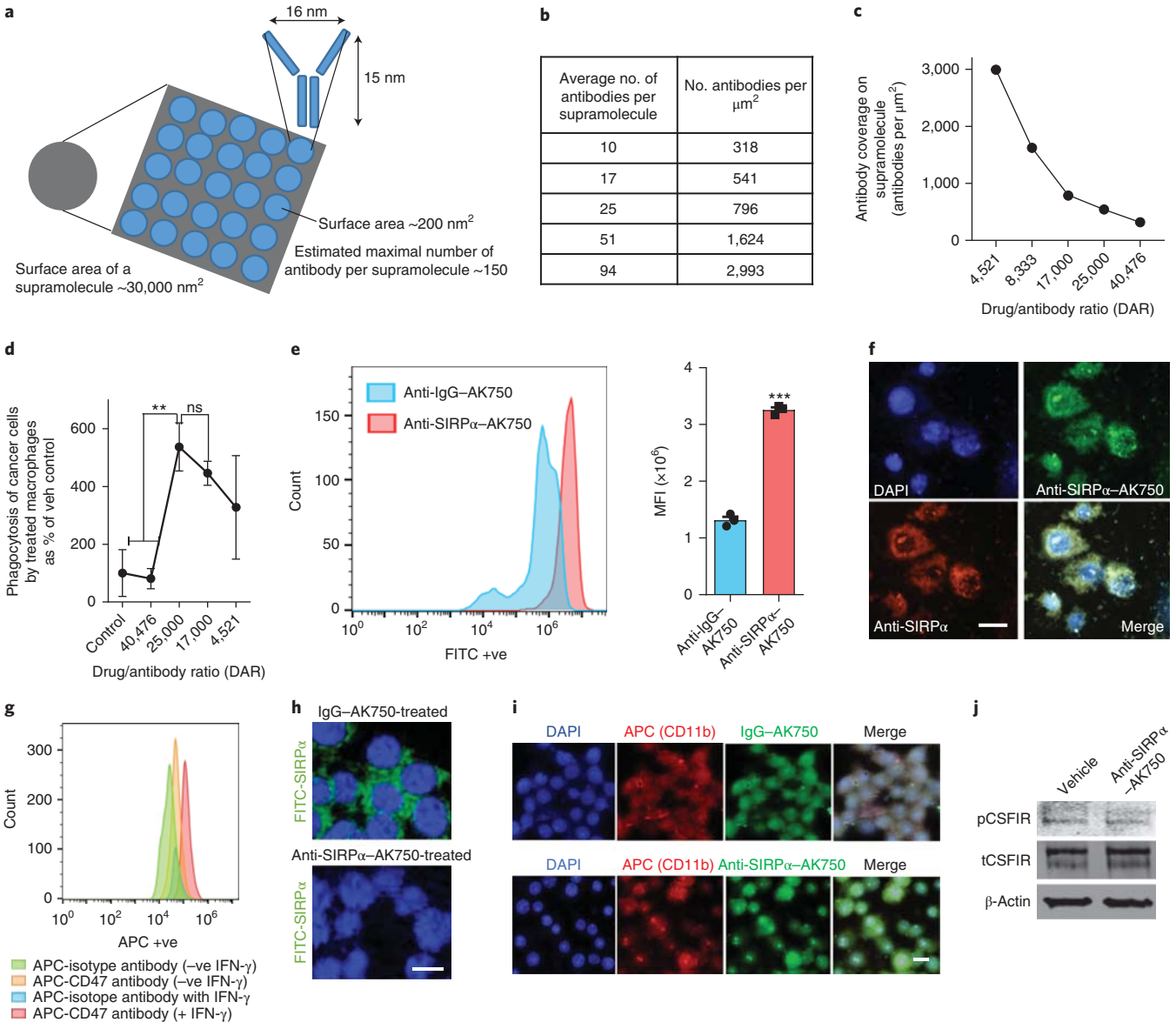

Average no. of antibodies per supramolecule	No. antibodies per μm²
10	318
17	541
25	796
51	1,624
94	2,993

Fig. 5 | Engineering a bifunctional anti-SIRPα–AK750 that blocks the CD47–SIRPα axis and CSF-1R. a, Theoretical model of the total surface area of a 100 nm supramolecule and maximal number of antibodies that can be accommodated on the surface. **b**, Total number of antibodies on a ~100 nm supramolecule and the corresponding surface density. **c**, The effect of increasing antibody concentration on the DAR. **d**, The effect of treatment with supramolecules with increasing antibody concentration but a constant number of CSF-1R-inhibiting amphiphiles on the phagocytosis of cancer cells by macrophages. RAW264.7 macrophages were stimulated with IL4 to first generate the M2 phenotype, and then incubated with anti-SIRPα–AK750. After 12 h incubation, CFSE-labelled B16/F10 melanoma cells were added to the culture, and incubated for 8 h. Nuclei were stained with DAPI (blue). Macrophages were labelled with APC-anti-CD11b antibody. AK750 was used as the control arm, and data shown are mean ± s.d. percentage change from AK750-treated group ($n = 3$) $^{**}p = 0.029$. **e**, Representative FACS data show increased binding of fluorophore-tagged anti-SIRPα–AK750 on TAMs as compared to control isotype IgG-AK750. The TAMs were isolated from the tumours of B16/F10 melanoma tumour-bearing mice using CD11b isolation kit. The macrophages were incubated with either FITC-tagged anti-SIRPα–AK750 or control FITC-tagged anti-IgG-AK750 for 4 h, followed by washing with cold PBS. Binding of the supramolecules was analysed using FACS. Graph shows the quantification of the binding and internalization of anti-SIRPα –AK750 to TAMs compared to control anti-IgG-AK750, as measured by mean fluorescence intensity (MFI) in TAMs. Data shown are mean ± s.e.m. ($n = 3$). $^{***}p < 0.001$ (Student's *t*-test, two-sided). **f**, Representative confocal images show binding of FITC-tagged anti-SIRPα–AK750 to SIRPα protein on M2 macrophages with anti-SIRPα–AK750. M2 macrophages were generated by stimulating RAW264.7 cells with IL4 followed by incubation with FITC-tagged anti-SIRPα–AK750 for 4 h. Nuclei were stained with DAPI (blue) and SIRPα protein was labelled with APC-anti-SIRPα antibody. **g**, Melanoma cells were treated with interferon gamma (IFNγ) to increase the expression of CD47 as seen using the FACS plot. **h**, The CD47-expressing cancer cells were incubated with fluorescently tagged SIRPα in the presence of anti-SIRPα–AK750 or control IgG–AK750. Confocal imaging reveals that the treatment with anti-SIRPα–AK750 completely inhibits the SIRPα-CD47 binding unlike the control IgG–AK750 supramolecules. **i**, Representative fluorescence images show internalization of FITC-tagged anti-SIRPα–AK750 in M2 macrophages. **j**, Western blot shows treatment with anti-SIRPα–AK750 decreases the levels of phosphor-CSF-1R without any change to total CSF-1R. Actin levels were used for normalization. RAW264.7 cells were stimulated with IL4 to generate the M2 phenotype, followed by incubation with anti-SIRPα–AK750. After 48 h of incubation, the cells were lysed and analysed using western blotting. The cropped blots are used in the figure, and full-length blots are presented in Supplementary Fig. 15. All scale bars, 10 μm.

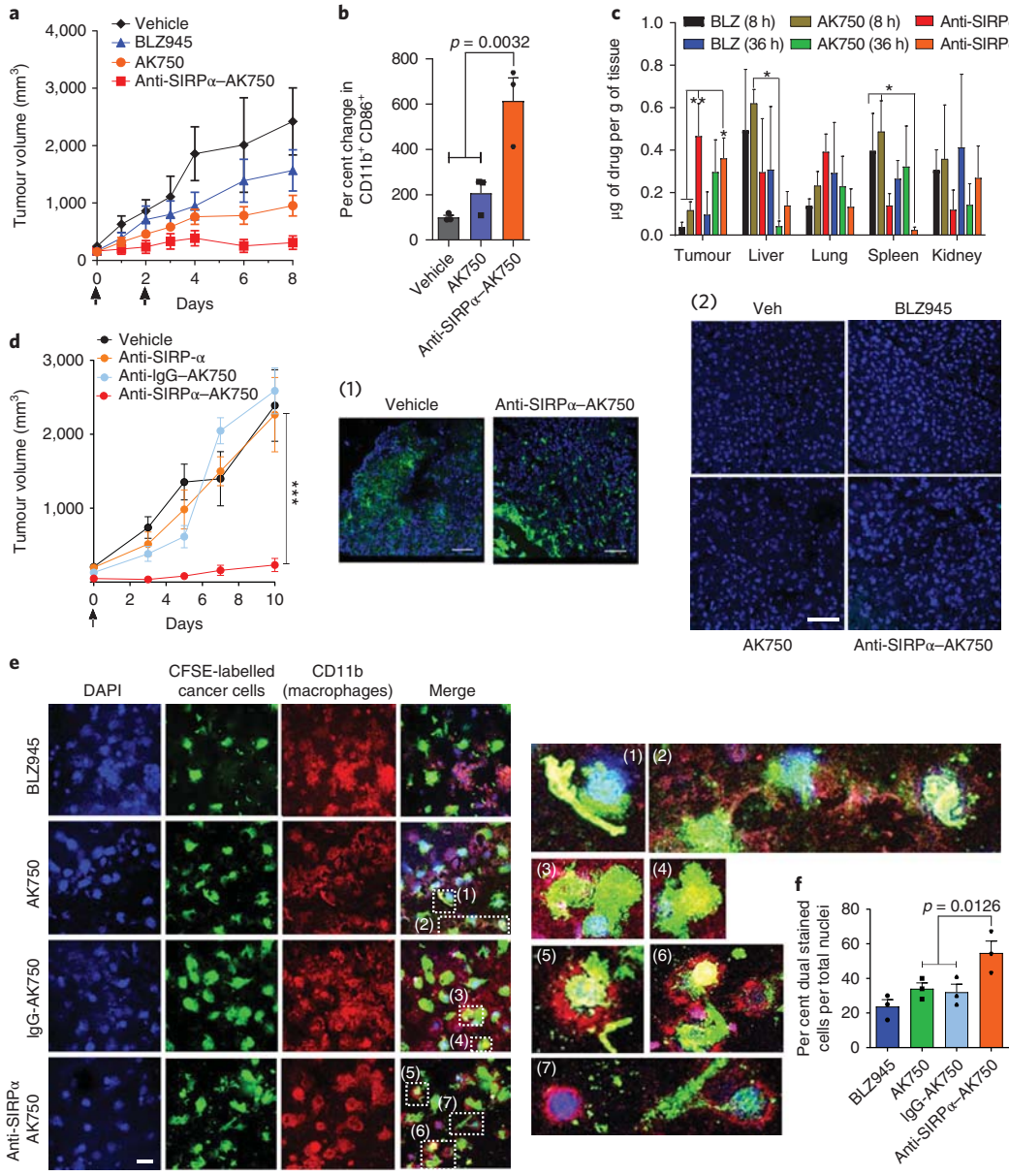

Fig. 6 | Single dose of anti-SIRPα–AK750 abrogates tumour growth in a syngeneic B-16/F10 melanoma C57BL/6 mouse model. a, Tumour growth curves show the effect of two cycles of treatment on tumour volume in a syngeneic B-16/F10 melanoma C57BL/6 mouse model. Animals with 75 mm^3 tumours were randomized into four treatment groups: (1) vehicle controls, (2) BLZ945 (45 mg kg^{-1}, i.p.), (3) AK750 (mole equivalent to BLZ945 dose), and (4) anti-SIRPα–AK750 (at mole equivalent to BLZ945 dose). One should note the different routes of administration; i.p. administration can result in lower bioavailability than i.v. Data shown are mean ± s.e.m. ($n = 5$). **b**, Graph shows the quantification of expression M1 markers ($CD11b^+CD86^+$) in single-cell suspensions of the harvested tumour post-treatment, as quantified using flow cytometry. Tumours were harvested on day 10 and single-cell suspensions prepared. Data shown are mean ± s.e.m. ($n = 3$), p value is shown (one-way ANOVA). **c**, Quantitative analysis of drug biodistribution in different organs. Major reticuloendothelial system (RES) organs were excised from tumour-bearing mice at different time points after a single injection of AK750, anti-SIRPα–AK750 and BLZ945. (All animals were dosed with drugs at a molar equivalent to 15 mg kg^{-1} dose of BLZ945, administered by i.v.) The drug concentrations per gram of tissue were quantified using LC/MS/MS. Error bars represent mean ± s.e.m. ($n = 3$) (one-way ANOVA). **d**, Tumour growth curves show the effect of a single cycle of treatment on tumour volume in a syngeneic B-16/F10 melanoma C57BL/6 mice model. Animals with 75 mm^3 tumours were randomized into four treatment groups: (1) vehicle controls, (2) anti-SIRPα–IgG (5 mg kg^{-1}), (3) IgG–AK750 (equivalent to a molar dose equivalent to 45 mg kg^{-1} of BLZ945), and (4) anti-SIRPα–AK750 (at a molar equivalent to AK750 dose used in group 3). Data shown are mean ± s.e.m. ($n = 5$), $***p < 0.001$ (one-way ANOVA). (1) Representative fluorescence images show $F4/80^+$ macrophages in cross-sections of tumour tissue from vehicle- and anti-SIRPα–AK750-treated groups. (2) Cross-sections of liver stained for apoptosis signal (TUNEL) show the absence of any toxicity signal. **e**, Representative confocal images show the effect of different treatments on phagocytosis of B16/F10 melanoma cells in a co-culture assay with macrophages. RAW264.7 cells were stimulated with IL4 to generate M2 phenotype, and then incubated with BLZ945, AK750, IgG–AK750 or anti-SIRPα–AK750. After 12 h incubation, CFSE-labelled B16/F10 melanoma cells were added to the culture, and incubated for 8 h. Nuclei were stained with DAPI (blue), macrophages were labelled with APC-anti-CD11b antibody. Images were captured using a confocal microscope at the same magnification. Scale bar, 10 μm. (1–7) Zoomed-in images from corresponding merged images show CFSE-labelled cancer cells (green) being phagocytosed by macrophages (red). **f**, Percentage of phagocytosis as determined by measuring the percentage of dual-stained cells (red and green) to total nuclei (blue). Data shown are mean ± s.e.m. ($n = 3$), p value is shown in the graph (one-way ANOVA followed by Newman–Keul's post-hoc test).

macrophages or cancer cells at the concentrations used in this study (Supplementary Fig. 8a–c).

AK750 exerts increased antitumour efficacy in melanoma and breast cancer. We next tested whether the in vitro observations translated into in vivo efficacy using two extremely aggressive, hard-to-treat syngeneic tumour models. In a recent study, we have demonstrated that supramolecular structures preferentially home into tumours, arising from the leaky pathophysiological neovasculature in the tumour. Consistent with these observations, we observed that a near-infrared, dye-tagged supramolecule indeed distributed across the tumour with time (Fig. 3a). Liquid chromatography–mass spectrometric (LC-MS) analysis revealed an almost eightfold increase in AK750 concentration in the tumour as opposed to BLZ945 when both were administered at the same molar doses in animals (Fig. 3b). To validate the therapeutic efficacy of AK750, we randomly sorted B16/F10 melanoma-bearing mice into three groups and treated each group with three cycles of one of the following: blank vehicle (control); AK750 or BLZ945. The mice injected with vehicle formed large tumours by day 10 (the start of treatment was considered day 0), and consequently were killed. The animals in the other groups were also killed at the same time point to evaluate the effect of the treatments on tumour pathology. As shown in Fig. 3c, while treatment with BLZ945 decreased tumour growth compared with vehicle-treated animals, treatment with AK750 resulted in a complete inhibition of tumour growth. Changes in body weight were within the acceptable limits (Fig. 3d). Western blot analysis of the tumours' lysate revealed a complete inhibition of CSF-1R phosphorylation in the tumours treated with AK750 (Fig. 3e). Furthermore, quantitative analysis of the TAMs using FACS revealed that treatment with AK750 significantly reduced M2 macrophage ($CD11b^+CD206^+$) and increased the M1 pool ($CD11b^+MHCII^+$, $CD80^+$, $CD86^+$), which could mechanistically explain the in vivo efficacy (Fig. 3f). We validated these observations in a second immunocompetent murine 4T1 breast cancer model for stage IV human breast cancer. Treatment was started when the tumours reached 75 mm^3 in volume (day 0). As shown in Fig. 4a and Supplementary Fig. 8d, treatment with AK750 significantly inhibited tumour growth in a dose-dependent manner. By contrast, an equimolar dose of BLZ945 had limited efficacy as did a therapeutic antibody against CSF1. The differences in response between the two tumour models are consistent with clinical observations, where melanoma responds better to immunotherapies compared to breast cancer. Interestingly, both AK750 and BLZ945 resulted in a reduction in metastatic nodes in the lungs, although the effect was significantly greater with the former (Fig. 4b). This is consistent with the pro-metastatic role played by TAMs in breast cancer[10]. Additionally, treatment with AK750 significantly increased survival as compared with BLZ945 (Fig. 4c). None of the treatments resulted in any change in body weight (Fig. 4d). Analysis of the TAMs using FACS for M2 markers and M1 markers revealed that AK750 treatment switched the tumour macrophage from an M2 to M1 contexture. Unlike the observations in melanoma, here BLZ945 failed to reduce M2 macrophages and had no effect on M1 markers, which could explain the differences observed in efficacy outcomes with BLZ945 in the two tumour models. Interestingly, treatment with AK750 increased the number of effector $CD4^+$ and $CD8^+$ T cells, which are implicated in exerting a cytotoxic effect in collaboration with M1 macrophages[3,26,27] (Fig. 4e–j). Taken together, the in vitro and in vivo results indicate that the improved pharmacodynamic effect, that is sustained inhibition of CSF1R, and the increased intratumoural bioavailability could underlie the improved antitumour efficacy seen with AK750.

Facile integration of SIRPα targeting to AK750. Having validated the enhanced CSF-1R-inhibiting function of AK750 compared with current clinical approaches of targeting CSF1 signalling, we next tested whether integrating the SIRPα-targeting function to the supramolecule can further increase the antitumour efficacy over and above that seen with AK750. The modularity of the system meant that we could display SIRPα-blocking antibodies on the surface of the supramolecule via simple conjugation to the terminal ends of the polyethylene glycol chains using a carbodiimide cross-linker chemistry. Theoretically, the surface area of a spherical supramolecule of ~100 nm diameter is ~30,000 nm^2, which means it can accommodate ~150 antibodies aligned parallel to each other (Fig. 5a). As the first step, we engineered the anti-SIRPα–AK750 supramolecules with increasing number of antibodies (Fig. 5b) while keeping the concentration of the CSF-1R-inhibiting amphiphiles per supramolecule constant. An analysis based on the average number of supramolecules in an aliquot indicated that each supramolecule comprises approximately 425,000 ± 149,000 molecules of the CSF-1R-inhibiting amphiphiles. Integrating between 10 to 94 antibodies per supramolecule (318–2,993 antibodies μm^{-2}), while keeping the concentration of AK750 constant, resulted in a drug/antibody ratio (DAR) ranging between ~4,521 to 40,476 (Fig. 5c). This is a significant improvement over classical ADCs, which typically have a DAR of 4–6 (ref. [28]). Next we tested the impact of this increasing antibody density on the phagocytosis of cancer cells by macrophages. The anti-SIRPα–AK750 supramolecules, with increasing numbers of SIRPα-blocking antibodies, were added to a co-culture of macrophages and cancer cells. As shown in Fig. 5d, a bell-shaped concentration-efficacy (phagocytosis) curve was obtained, with maximal phagocytosis achieved at a density of 541 antibodies μm^{-2}. The degree of phagocytosis was statistically similar between 541 antibodies μm^{-2} and 796 antibodies μm^{-2} but decreased at 1,624 antibodies μm^{-2}, which could arise from steric hindrances. We conducted further studies with supramolecules with 796 antibodies μm^{-2}, which translated to 25 ± 9 antibodies per supramolecule, based on the rationale that a higher antibody coverage increases the probability of binding in a dynamic system. The total incorporation efficiency of the CSF-1R-inhibiting amphiphile in the anti-SIRPα–AK750 supramolecule was calculated to be 76 ± 5%, statistically not different from that achieved in the case of the AK750 supramolecule (83 ± 2%) (Supplementary Fig. 9a), consistent with the modularity of the system that allows addition of functionality without impacting the basic composition. The hydrodynamic diameter of this bi-functional supramolecule was found to increase marginally to ~180 ± 27 nm (Supplementary Fig. 9b). The surface charge (zeta potential) was calculated to be −17 ± 8 mV. Neither size nor surface charge varied significantly over a seven-day period indicating that the bifunctional supramolecules are stable (Supplementary Fig. 9c). Furthermore, less than 20% of the total CSF-1R-inhibiting amphiphile was found to be released over the study period at physiological pH 7.4, consistent with that observed earlier in the case of AK750 supramolecules. In contrast, a sustained, >80% release was observed when the supramolecules were incubated with macrophage cell lysate (Supplementary Fig. 9d). To test the serum stability, we incubated the anti-SIRPα–AK750 supramolecule in increasing concentration of human serum and quantified the change in diameter over time. No statistical change in diameter was observed over 24 hours, but a serum-concentration-dependent increase was evident at later time points, consistent with corona formation (Supplementary Fig. 9e).

Enhanced binding of the anti-SIRPα–AK750 to macrophages. To validate whether the bifunctional supramolecule binds to SIRPα on macrophages, we incubated TAMs isolated from B16/F10 melanoma-bearing mice with anti-SIRPα–AK750 or control IgG–AK750 that were fluorophore-tagged. At the end of four hours of incubation, the cells were washed with cold phosphate-buffered saline (PBS) and analysed using flow cytometry, which revealed significantly enhanced binding of the anti-SIRPα–AK750 as compared to control IgG–AK750 (Fig. 5e). Additionally, immunolabelling the

TAMs for SIRPα followed by fluorescence microscopy revealed a colocalization of the signals from fluorophore-tagged anti-SIRPα–AK750 and SIRPα (Fig. 5f), which further validated the binding of the supramolecule to SIRPα. To test whether anti-SIRPα–AK750 blocks the SIRPα–CD47 axis, we treated melanoma cells with interferon gamma (IFNγ) to increase the expression of CD47, and then added fluorescently tagged SIRPα to the cells in the presence of anti-SIRPα–AK750 or control IgG–AK750. Confocal imaging revealed that the treatment with anti-SIRPα–AK750 completely inhibited SIRPα–CD47 binding unlike the control IgG–AK750 supramolecules (Fig. 5g,h). Ligation to SIRPα can potentially inhibit phagocytosis[14]. Given that cellular internalization is critical for the anti-SIRPα–AK750 to inhibit CSF-1R, we next tested whether binding to SIRPα induces the internalization of the supramolecule into the cell. As shown in Fig. 5i, we observed greater internalization within the macrophages within four hours of incubation as compared with a control IgG-coupled AK750. Furthermore, western blotting revealed a significant inhibition of phosphorylation of CSF-1R in macrophages treated with anti-SIRPα–AK750 (Fig. 5j).

Anti-SIRPα–AK750 increases phagocytosis of cancer cells and anticancer efficacy. We next tested whether the anti-SIRPα–AK750 treatment results in a greater antitumour effect than AK750 *in vivo* using the aggressive B16/F10 melanoma model. As three cycles of AK750 maximally ablated tumour growth, we first treated tumour-bearing animals with two cycles of treatment. At this dose, AK750 submaximally inhibited tumour growth. The integration of the anti-SIRPα activity to the AK750 supramolecules significantly increased the antitumour efficacy as compared with AK750 or BLZ945 treatments (Fig. 6a). Analysing the TAMs revealed that the treatment with anti-SIRPα–AK750 significantly increased the M1 phenotype as compared with AK750 treatment (Fig. 6b). Interestingly, the bifunctional anti-SIRPα–AK750 exerted a greater anticancer efficacy than a combination of SIRPα-blocking antibody and AK750 (Supplementary Fig. 10a). We used a dose of 5 mg kg^{-1} for the anti-SIRPα antibody, which for a mouse of 20 g translates to ~4×10^{14} molecules. Similarly, we injected AK750 equivalent to ~1.3×10^{18} molecules of the CSF1-R-inhibiting amphiphile per 20 g mouse. The dosing of anti-SIRPα–AK750 translated to ~1.3×10^{18} molecules of the amphiphile and 7.5×10^{13} antibodies (based on a DAR of 17,000). One should note that a classical ADC-based approach using the same number of anti-SIRPα antibody as used in the anti-SIRPα–AK750 would have translated to ~4.5×10^{14} (at a DAR of 2) to 4.5×10^{14} (at a DAR of 6) molecules of the CSF-1R-inhibitor, which is significantly lower than the ~1.3×10^{18} molecules that was achieved with the supramolecular approach. A lower amount of antibody is therefore able to exert a greater effect when engineered together with the CSF-1R-inhibiting amphiphile in the same supramolecular construct as opposed to a combination of two separate entities. This is consistent with our recent observations, where bifunctional 2-in-1 supramolecules exerted greater efficacy than the simple combinations of two therapeutic agents. We demonstrated that two therapeutic agents can stochastically distribute within the tumour independent of each other such that subsets of target cells are exposed to only one of the therapeutic agents, which lowers the total efficacy. By contrast, bifunctional 2-in-1 supramolecules ensure that both therapeutic agents are presented to the same cell[29]. Additionally, we rationalized that the anti-SIRPα component could confer a tumour-homing functionality to the supramolecule. To test this, we next performed biodistribution studies, where animals were injected with AK750 or anti-SIRPα–AK750, and the levels of AK750 in different tissues was detected using LCMS. As shown in Fig. 6c, anti-SIRPα–AK750 treatment resulted in a significantly greater build-up of the drug in the tumour at an early time-point (8 h) as compared with AK750. While this distinction between AK750 and anti-SIRPα–AK750 was lost at a late time-point, the total intratumoural drug concentration reached with the anti-SIRPα–AK750 was twofold that reached with AK750 within 36 h. Both treatments resulted in greater intra-tumoural concentrations than BLZ945. Furthermore, pharmacokinetic studies revealed that unlike AK750, anti-SIRPα–AK750 exhibited a bell-shaped plasma concentration-time curve, suggestive of a reservoir to which the anti-SIRPα-supramolecule binds at earlier time-point. Taken together with the biodistribution data, this result is consistent with the binding of anti-SIRPα–AK750 to circulating and tumour macrophages/monocytes, which could also explain the longer half-life (Supplementary Fig. 10b,c). The delayed accumulation of AK750 in the tumour is consistent with the ability of nanoparticles to passively home into tumours over time due to an enhanced permeability and retention effect[30]. Based on the pharmacokinetic studies, we rationalized the synergistic anti-cancer effect seen with the bifunctional anti-SIRPα–AK750 over AK750 can be best dissected with a single dose of the drug as repeat dosing within short time-intervals could result in saturation kinetics, where the CSF-1R inhibition could mask the impact of the SIRPα inhibition. Indeed, as shown in Fig. 6d, a single dose of anti-SIRPα–AK750 resulted in a dramatic inhibition of tumour progression. By contrast, a single dose of anti-SIRPα antibody had minimal effect on the tumour progression, while the single dose of control IgG–AK750 resulted in an initial delay in tumour progression with tumour rebound seen at later time points. None of the treatments resulted in any off-target toxicity to the organs studied, as quantified using TUNEL staining, which labels apoptotic cells (Fig. 6d(2), Supplementary Fig. 10d). We did not see depletion of F4/80$^+$ cells in the tumours treated with anti-SIRPα–AK750 as compared to vehicle control, consistent with recent observations (Fig. 6d(1))[31]. To further understand the increased efficacy with anti-SIRPα–AK750 at a mechanistic level, we loaded B16/F10 melanoma cells with a cell-impermeant CFSE dye and incubated them for eight hours with macrophages that were pretreated with the supramolecules or BLZ945. As shown in Fig. 6e,f, treatment with anti-SIRPα–AK750 significantly increased the phagocytosis of cancer cells by macrophages as compared with either IgG–AK750 or BLZ945 treatments. Additionally, the treatments exerted a direct inhibitory effect on the tumour cells only at very high concentrations exceeding the levels we used for the study (Supplementary Fig. 11a,b). However, even at the highest concentrations, we did not observe any significant apoptosis of macrophages (Supplementary Fig. 11c). Taken together, these results indicate that the anti-SIRPα component of anti-SIRPα–AK750 can facilitate the targeting of TAMs. The inhibition of the 'eat me not' signal synergizes with the repolarization of TAMs to the M1-phenotype resulting from CSF-1R inhibition to exert enhanced anticancer effects compared with AK750 treatment alone.

Several components of the bifunctional supramolecule can advance immunotherapy in humans. First, the ability of supramolecules to accumulate in the tumour, resulting from increased bioavailability, together with the homing to SIRPα on the TAMs, could result in greater intratumoural concentrations and minimize off-target toxicity, and translate into an improved therapeutic index. Second, the supramolecule induces a sustained inhibition of CSF-1R and key downstream signalling cascades, resulting in enhanced antitumour efficacy and reduced metastasis in aggressive tumour models compared with current clinical-stage inhibitors of MCSF–CSF-1R axis. Third, it is increasingly being realized that combination immunotherapy, including blocking two distinct targets in the same immune cell, is the future of immuno-oncology. For example, in recent clinical studies, targeting programmed cell death protein 1 (PD1) and cytotoxic T-lymphocyte-associated protein 4 (CTLA4) on T cells with the combination of a standard dose of pembolizumab together with a reduced dose of ipilimumab, respectively, was found to increase anticancer efficacy without amplifying the side effects[32]. Our results with the SIRPα–AK750 supramolecule lays the groundwork for a combination approach targeting both CD47–SIRPα and

MCSF–CSF-1R signalling axes simultaneously, rather than targeting a single axis, to maximally activate macrophages in immunooncology. The fact that a single cycle of the SIRPα–AK750 supramolecule exerted significant tumour inhibition suggests that such an approach may allow the reduction in total dose without losing efficacy. Although the supramolecules induce a dramatic repolarization of TAMs from an M2 to M1 phenotype, an associated increase in phagocytosis of cancer cells and enhanced antitumour efficacy, it is likely that the macrophage-activating supramolecules will have to be combined with immune checkpoint inhibitors that can enable T cells to respond efficiently to antigen presentation by macrophages. Such an integrative immunotherapy approach underpinned by bifunctional supramolecules can emerge as a new paradigm in the treatment of cancer.

Methods

Detailed methods are described in the Supplementary Information.

Synthesis and characterization of anti-SIRPα-AK750. CSF-1R inhibiting amphiphile was synthesized by conjugating BLZ945 with cholesteryl hemisuccinate using an EDC and DMAP coupling reaction as described in the Supplementary Methods. The products were characterized by ^{1}H NMR spectroscopy and mass spectrometry. For supramolecule synthesis, 20 mol% of CSF-1R inhibiting amphiphile, 30 mol% of 1,2-distearoyl-*sn*-glycero-3-phosphoethanolamine-*N*-[carboxy(polyethylene glycol)-2000] and 50 mol% L-α-phosphatidylcholine was dissolved in 1 ml of DCM. The solvent was evaporated into a thin and uniform film using a rotary evaporator. The film was then hydrated with 1.0 ml H_2O for 1.5 h at 60 °C. After hydration, one equivalent of EDC and NHS were each added and incubated at room temperature for 2 h. To the samples, 4 µl (0.5 mg kg^{-1} concentration) of either IgG (control) or anti-SIRPα antibodies were added and the samples were incubated at 4 °C for 12 h. We used a well-characterized anti-SIRPα blocking IgG antibody (BioLegend, AB_11203723). After incubation, the samples were extruded at 60 °C using a 400 nm and then a 200 nm PC membrane with 500 µl sample volume to obtain sub-200 nm particles. The samples were further passed through a Sephadex G-25 column to remove free molecular subunits and non-conjugated antibodies. The physical stability of the nanoparticles was evaluated by measuring changes in mean particle size and ζ potential during storage at 4 °C.

Quantum-mechanical all-atomistic simulations. An all-atomistic simulation was performed to elucidate the stability of the supramolecular structures. Briefly, geometry optimization using quantum-mechanical methods was performed to obtain the lowest energy conformation of the molecular subunit or BLZ945. Following the force field development step, the subunit was energy optimized using the developed force field using the steepest descent algorithm. Quantum-mechanical geometry-optimized structures were considered as the starting structure for MD simulations. BLZ945 and CSF-1R inhibiting molecular subunit molecules were inserted inside the lipid bilayer structure and equilibrated till 10 ns for all the systems to randomize. Models were constructed such that the system contained 256 molecules of co-lipid and 64 molecules of the geometry-optimized structure of the molecular subunit. The trajectories were analysed as described in the Supplementary Information.

In vitro macrophage polarization assays. The supramolecules were tested on both primary and cell line cultures, in vitro, under different conditions described in the Supplementary Information. The efficacy was quantified using western blotting or flow cytometry.

In vitro phagocytosis assay. 5×10^4 RAW264.7 cells were plated per well in an eight-well chamber slide. After 24 h of IL-4 (20 ng ml^{-1}) stimulation, anti-Sirpa-AK750, AK750, IgG-AK750 and BLZ945 free drug were added at 67 nM (equivalent to the BLZ-945 concentration) to macrophages and incubated for 3 h at 37 °C. The macrophages were labelled with APC anti-CD11b antibody. B16/F10 melanoma cells (5×10^4) were labelled with CFSE as per the manufacturer's protocol and added to macrophages at a 1:1 ratio and incubated for 8 h. The imaging was performed with an Olympus confocal microscope. The images were analysed and quantification was performed using ImageJ software.

In vivo efficacy studies. B16/F10 melanoma cells (1×10^5) or 4T1 cells were implanted subcutaneously in the flanks of 4–6-week-old C57BL/6 male mice or female BALB/c mice, respectively (Charles River Laboratories). When the tumour volume reached a predefined size (~50 mm^3), the animals were randomized into different treatment groups. The animals were administered via tail vein with following treatments as described in the Supplementary Information. The tumour volume was calculated with the formula, $L\times B^2/2$, where the L and B are the longest and the shortest diameter, respectively, as measured using a vernier caliper. Animals were killed once the tumours in the vehicle-treated group reached a predetermined cut-off or sign of any distress. The tumour tissues were harvested for further immune characterization. All animal procedures were approved by the Harvard Institutional Use and Care of Animals Committee.

Reporting Summary. Further information on experimental design is available in the Nature Research Reporting Summary linked to this article.

Data availability. The authors declare that all data supporting the findings of this study are available within the paper and its Supplementary Information.

Received: 9 June 2017; Accepted: 17 May 2018;
Published online: 2 July 2018

References

1. Mantovani, A., Marchesi, F., Malesci, A., Laghi, L. & Allavena, P. Tumour-associated macrophages as treatment targets in oncology. *Nat. Rev. Clin. Oncol.* **14**, 399–416 (2017).
2. Engblom, C., Pfirschke, C., & Pittet, M. J. The role of myeloid cells in cancer therapies. *Nat. Rev. Cancer* **16**, 447–462 (2016).
3. Noy, R., & Pollard, J. W. Tumor-associated macrophages: from mechanisms to therapy. *Immunity* **41**, 49–61 (2014).
4. Condeelis, J., & Pollard, J. W. Macrophages: obligate partners for tumor cell migration, invasion, and metastasis. *Cell* **124**, 263–266 (2006).
5. Gabrilovich, D. I., Ostrand-Rosenberg, S. & Bronte, V. Coordinated regulation of myeloid cells by tumours. *Nat. Rev. Immunol.* **12**, 253–268 (2012).
6. Grivennikov, S. I., Greten, F. R., & Karin, M. Immunity, inflammation, and cancer. *Cell* **140**, 883–899 (2010).
7. Biswas, S. K. & Mantovani, A. Macrophage plasticity and interaction with lymphocyte subsets: cancer as a paradigm. *Nat. Immunol.* **11**, 889–896 (2010).
8. Mosser, D. M. & Edwards, J. P. Exploring the full spectrum of macrophage activation. *Nat. Rev. Immunol.* **8**, 958–969 (2008).
9. Sica, A. et al. Macrophage polarization in tumour progression. *Sem. Cancer Biol.* **18**, 349–355 (2008).
10. Qian, B. Z. & Pollard, J. W. Macrophage diversity enhances tumor progression and metastasis. *Cell* **141**, 39–51 (2010).
11. Ruffell, B. & Coussens, L. M. Macrophages and therapeutic resistance in cancer. *Cancer Cell* **27**, 462–472 (2015).
12. Ries, C. H. et al. Targeting tumor-associated macrophages with anti-CSF-1R antibody reveals a strategy for cancer therapy. *Cancer Cell* **25**, 846–859 (2014).
13. Pyonteck, S. M. et al. CSF-1R inhibition alters macrophage polarization and blocks glioma progression. *Nat. Med.* **19**, 1264–1272 (2013).
14. Chao, M. P., Weissman, I. L. & Majeti, R. The CD47-SIRPα pathway in cancer immune evasion and potential therapeutic implications. *Curr. Opin. Immunol.* **24**, 225–232 (2012).
15. McCracken, M. N., Cha, A. C. & Weissman, I. L. Molecular pathways: activating T cells after cancer cell phagocytosis from blockade of CD47 "don't eat me" signals. *Clin. Cancer Res.* **21**, 3597–3601 (2015).
16. Beck, A., Goetsch, L., Dumontet, C. & Corvaia, N. Strategies and challenges for the next generation of antibody–drug conjugates. *Nat. Rev. Drug Discov.* **16**, 315–337 (2017).
17. Garber, K. Bispecific antibodies rise again. *Nat. Rev. Drug Discov.* **13**, 799–801 (2014).
18. Kulkarni, A. et al. Algorithm for designing nanoscale supramolecular therapeutics with increased anticancer efficacy. *ACS Nano* **10**, 8154–8168 (2016).
19. Kulkarni, A., Natarajan, S. K., Chandrasekar, V., Pandey, P. R. & Sengupta, S. Combining immune checkpoint inhibitors and kinase-inhibiting supramolecular therapeutics for enhanced anticancer efficacy. *ACS Nano* **10**, 9227–9242 (2016).
20. Kulkarni, A. A. et al. Supramolecular nanoparticles that target phosphoinositide-3-kinase overcome insulin resistance and exert pronounced antitumor efficacy. *Cancer Res.* **73**, 6987–6997 (2013).
21. Zhou, D. et al. Macrophage polarization and function with emphasis on the evolving roles of coordinated regulation of cellular signaling pathways. *Cell. Signal.* **26**, 192–197 (2014).
22. Wilson, H. M. SOCS proteins in macrophage polarization and function. *Front. Immunol.* **5**, 357, (2014).
23. Ruffell, B., Affara, N. I. & Coussens, L. M. Differential macrophage programming in the tumor microenvironment. *Trends Immunol.* **33**, 119–126 (2012).
24. Whyte, C. S. et al. Suppressor of cytokine signaling (SOCS)1 is a key determinant of differential macrophage activation and function. *J. Leukoc. Biol.* **90**, 845–854 (2011).
25. Genin, M., Clement, F., Fattaccioli, A., Raes, M. & Michiels, C. M1 and M2 macrophages derived from THP-1 cells differentially modulate the response of cancer cells to etoposide. *BMC Cancer* **15**, 577 (2015).
26. Gajewski, T. F., Schreiber, H. & Fu, Y. X. Innate and adaptive immune cells in the tumor microenvironment. *Nat. Immunol.* **14**, 1014–1022 (2013).

27. Ruffell, B. et al. Macrophage IL-10 blocks $CD8^+$ T cell-dependent responses to chemotherapy by suppressing IL-12 expression in intratumoral dendritic cells. *Cancer Cell* **26**, 623–637 (2014).
28. Diamantis, N. & Banerji, U. Antibody-drug conjugates–an emerging class of cancer treatment. *Br. J. Cancer* **114**, 362–367 (2016).
29. Goldman, A. et al. Rationally designed 2-in-1 nanoparticles can overcome adaptive resistance in cancer. *ACS Nano* **10**, 5823–5834 (2016).
30. Sengupta, S. Cancer nanomedicine: lessons for immuno-oncology. *Trends Cancer* **3**, 551–560 (2017).
31. Gholamin, S. et al. Disrupting the CD47-SIRPà anti-phagocytic axis by a humanized anti-CD47 antibody is an efficacious treatment for malignant pediatric brain tumors. *Sci. Transl. Med.* **9**, eaaf2968 (2017).
32. Long, G. V. et al. Standard-dose pembrolizumab in combination with reduced-dose ipilimumab for patients with advanced melanoma (KEYNOTE-029): an open-label, phase 1b trial. *Lancet Oncol.* **18**, 1202–1210 (2017).

Acknowledgements

This work was supported by a DoD Breakthrough Award (BC132168), an American Lung Association Innovation Award (LCD-259932-N), and an NCI UO1 (CA214411) to S.S. and a National Cancer Institute of the National Institutes of Health (P50CA168504) and Hearst Foundation/Brigham and Women's Hospital Young Investigator Award to A.K. The authors would like to thank the Dana Farber Cancer Institute Flow Cytometry Core Facility for their expertise, consulting and assistance with flow cytometry experiments. The authors would like to thank the Mass Spectrometry Core Facility and Biophysical Characterization Core Facility at the Institute for Applied Life Sciences (IALS), University of Massachusetts Amherst for consultation and assistance with mass spectrometry experiments.

Author contributions

A.K. conceived the idea, designed the experiments and mentored the research. P.P. performed the molecular dynamics simulation studies. V.C., S.K.N. and A.R. performed the supramolecule synthesis and characterization. V.C., S.K.N., A.R., J.N., H.B. and D.A. performed in vitro experiments. A.K.A. helped with confocal imaging. A.K., V.C., S.K.N. and A.R. performed in vivo experiments. A.K. and S.S. wrote the paper and received comments and edits from all the authors.

Competing interests

S.S. is a cofounder and holds equity in Akamara Therapeutics, which is developing supramolecular therapeutics, and holds equity in Mitra Biotech, which is developing cancer diagnostics.

Additional information

Supplementary information is available for this paper at https://doi.org/10.1038/s41551-018-0254-6.

Reprints and permissions information is available at www.nature.com/reprints.

Correspondence and requests for materials should be addressed to A.K. or S.S.

Publisher's note: Springer Nature remains neutral with regard to jurisdictional claims in published maps and institutional affiliations.